Numerical Analysis of In-flight Particles in Plasma Jet with an Externally Applied Magnetic Field

Hiroki SAITO*, Yusuke NAKANE*, Takayasu FUJINO* and Hidemasa TAKANA**

* Department of Engineering Mechanics and Energy, University of Tsukuba
1-1-1 Tennodai, Tsukuba, Ibaraki, 305-8577, Japan
E-mail: tfujino@kz.tsukuba.ac.jp

** Institute of Fluid Science, Tohoku University
2-1-1 Katahira, Aoba-ku, Sendai, Miyagi, 980-8577, Japan

Received 17 March 2016

In this work, three-dimensional, time-dependent magnetohydrodynamic (MHD) simulations of a direct-current (dc) plasma spray with an externally applied magnetic field are performed, and also the trajectories and heating histories of in-flight particles in a plasma spray jet are analyzed by Lagrangian method with one-way coupling between particle and plasma jet. The working gas is pure argon (Ar) and the material of in-flight particles is zirconium dioxide (ZrO_2). The representative values of operating current and magnetic flux density of externally applied magnetic field in this work are 350 A and 0.8 T, respectively. Numerical results obtained in the MHD simulation demonstrate that the use of externally applied magnetic field yields the rotation of the arc root on the anode. This rotation generates a plasma jet with a swirling component. Furthermore, it is shown from the numerical results that applying the magnetic field increases the operating voltage and thus boosts an amount of input power compared to the one without applying it. The analytical results of in-flight particles suggest that the impact positions of in-flight particles on the substrate in the case with the externally applied magnetic field change temporally due to the swirling component of the plasma jet, even when the injected position of particles is fixed. However, the utilization of externally applied magnetic field enhances heat transfer to particles, which leads to impacting of particles on substrate with well-molten state because of higher enthalpy plasma jet.

Key words : Thermal plasma, Plasma jet, Particle trajectory, Externally applied magnetic field, Arc rotation

1. Introduction

Plasma spray is one of the well-established coating technologies which have been widely used to give materials special properties resistant to wear, corrosion, and high-temperature, etc. An injected working gas is heated and accelerated by an arc between anode and cathode in a plasma torch, coming out as plasma jet from the torch nozzle. Microsized powder particles injected into the plasma jet get momentum with molten state, impacting on a substrate and generating coatings.

It is well known that coating quality is strongly influenced by arc fluctuation inside the plasma torch (Pfender, 1999), which is attributed to periodic or chaotic movement of anode arc root (Wutzke *et al*., 1967; Wutzke *et al*., 1968). The arc fluctuation changes temperature and velocity distributions of plasma jet at the torch outlet with time; in some cases, this fluctuation would lead to unmelted particles, and thus low spraying efficiency and poor coating quality. However, a stationary arc is undesirable because a heat transferred from arc to anode is too high, resulting in decreasing anode lifetime. Therefore, for realizing high coating quality at low cost, it is desirable to improve the controllability of anode arc root movement.

One of several methods suggested for improving is to utilize externally applied magnetic field both numerically and experimentally (Sato *et al*., 2001; Hu *et al*., 2013; Mostaghimi and Boulos, 2015). Figure 1 shows the schematic diagram of the plasma torch developed by Pershin *et al* (2013). A solenoid coil for producing externally applied magnetic field is placed around the anode. The Lorentz force induced by the interaction between the arc and the magnetic field rotates the

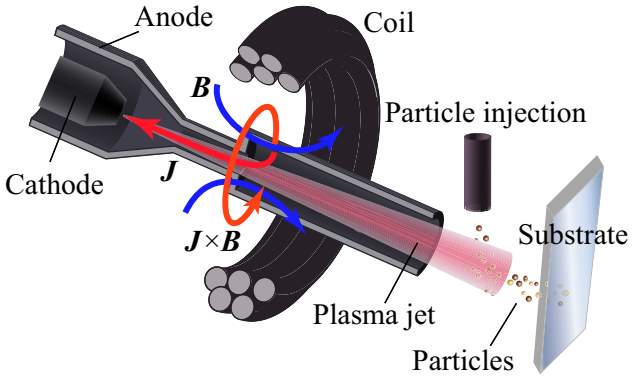

Fig. 1 Schematic diagram of plasma torch with externally applied magnetic field.

anode arc root. This rotational movement would be expected to help mitigate the heat load to the anode wall and improve the controllability of anode arc root movement.

A lot of three-dimensional simulations have been reported to study the complex arc movement and the in-flight particle trajectories (for example, Li and Pfender, 2007; Trelles, 2013; Shang *et al*., 2014; Alaya *et al*., 2015). However, only a few studies have been conducted focusing on in-flight particles in a plasma jet with externally applied magnetic field considering interaction between plasma structure and in-flight particles (Nishiyama *et al*., 1999; Sato *et al*., 2003). These simulations have been conducted under axisymmetric two-dimensional approximation. In this work, therefore, we examine the effect of externally applied magnetic field on the fluid and electro dynamic characteristics of a plasma jet by means of three-dimensional, time-dependent magnetohydrodynamic simulation, and also we analyze the trajectories and heating histories of in-flight particles in the plasma jet using the Lagrangian method with one-way coupling between in-flight particles and plasma jet.

2. Mathematical model

2.1. Governing equations for plasma flow

The mathematical plasma flow model is based on a fully coupled treatment of flowfield together with electromagnetic field. The model is based on the following assumptions:

- Working gas is pure argon (Ar).
- Ar plasma flow is considered as compressible because its Mach number is about 0.7 in maximum.
- Ar plasma flow is laminar under local thermodynamic equilibrium (LTE) and local chemical equilibrium (LCE) states.
- Thermodynamic and transport properties of Ar plasma depend on gas temperature and pressure.
- The quasi-neutrality condition holds.
- Ar plasma is optically thin. The absorption of radiation is assumed to be negligible.
- The gravitational effect and the Hall effect can be neglected.

The Reynolds number estimated in the calculation domain is over 2000 in maximum. Therefore, a turbulent model will be implemented in our future study. The governing equations for flowfield, which are composed of mass, momentum, and total energy conservation equations, are written as follows:

Mass conservation equation

$$\frac{\partial}{\partial t}\int_V \rho dV + \oint_S \rho \boldsymbol{u}\cdot\boldsymbol{n}dS = 0 \tag{1}$$

Momentum conservation equations

$$\frac{\partial}{\partial t}\int_V \rho \boldsymbol{u}dV + \oint_S \rho \boldsymbol{u}\boldsymbol{u}\cdot\boldsymbol{n}dS = \int_V (\boldsymbol{J}\times\boldsymbol{B})dV - \oint_S p\boldsymbol{n}dS + \oint_S (\bar{\bar{\tau}}\cdot\boldsymbol{n})dS \tag{2}$$

Total energy conservation equation

$$\frac{\partial}{\partial t}\int_V \rho E_{flu}dV + \oint_S \rho H_{flu}\boldsymbol{u}\cdot\boldsymbol{n}dS = \oint_S \kappa(\nabla T\cdot\boldsymbol{n})dS + \int_V (\boldsymbol{J}\cdot\boldsymbol{E} - \dot{q}_{rad})dV + \oint_S (\bar{\bar{\tau}}\cdot\boldsymbol{u})\cdot\boldsymbol{n}dS \tag{3}$$

where the specific total energy E_{flu} and the specific total enthalpy H_{flu} are defined, respectively, as

$$E_{flu} = e_{flu} + \frac{|\boldsymbol{u}|^2}{2} \tag{4}$$

$$H_{flu} = E_{flu} + \frac{p}{\rho} \tag{5}$$

These conservation equations are discretized using the upwind finite volume method, in which the advection upstream splitting method (AUSM)-DV scheme (Wada and Liou, 1994) and the second-order central differential scheme are utilized for evaluating the numerical flux of convective and diffusion terms, respectively. The time integration is performed by the lower-upper symmetric Gauss-Seidel scheme (Yoon and Jameson, 1988).

For electromagnetic modeling, MHD approximation is adopted in this study. Under the approximation, the governing equations for electromagnetic field can be written as follows:

Generalized Ohm's law

$$\boldsymbol{J} = \sigma(\boldsymbol{E} + \boldsymbol{u} \times \boldsymbol{B}) \tag{6}$$

Maxwell's equations

$$\boldsymbol{E} = -\nabla\phi \tag{7}$$

$$\nabla \cdot \{\sigma(-\nabla\phi + \boldsymbol{u} \times \boldsymbol{B})\} = 0 \tag{8}$$

$$\boldsymbol{B} = \nabla \times \boldsymbol{A} + \boldsymbol{B}_0 \tag{9}$$

$$\Delta\boldsymbol{A} = -\mu_0 \boldsymbol{J} \tag{10}$$

Each of Eqs. (8) and (10) is discretized with the Galerkin finite element method, and then the derived linear equations on the potential ϕ and the vector potential $\boldsymbol{A}$ are solved with Bi-CGSTAB2 method (Gutknecht, 1993).

The computational program for plasma flow used in the present work showed its validity in the simulation for voltage variations of a rotary arc in a gas circuit breaker with externally applied magnetic field (Hirayama *et al.*, 2016).

2.2. Particle governing equations for in-flight particle's trajectory and heating history

For modeling the behavior of in-flight particles, the following assumptions are adopted:

- The shape of in-flight particles is spherical.
- The pertinent Biot number is at most 0.25, less than unity, and consequently the temperature gradient within the particles is negligible.
- The effect of particle behavior on plasma jet characteristics and the particle-particle interaction are negligible.

In-flight particles are driven by the drag, the pressure gradient, the added mass, the Basset history, the thermophoretic, the gravitational, the Saffman lift, and the Magnus lift forces. Most of these forces have little effect on particle motion because the mass density of plasma jet is much smaller than that of injected particles and the particle radius is very small. According to Pfender and Lee (1985), the drag force and the thermophoretic force are the main driving forces for particle motion. Thermophoretic force becomes important in regions with high temperature gradient, such as in the vicinity of substrate which will be included in our future simulation. The particle trajectory and heating history are obtained by solving the following equations (Li and Chen, 2002):

Equations of particle motion

$$\frac{d\boldsymbol{x}_p}{dt} = \boldsymbol{u}_p \tag{11}$$

$$\frac{d\boldsymbol{u}_p}{dt} = \left(\frac{3\rho C_D}{8 r_p \rho_p}\right) \cdot |\boldsymbol{u} - \boldsymbol{u}_p|(\boldsymbol{u} - \boldsymbol{u}_p) - 9\left(\frac{\mu^2}{\rho\rho_p r_p^2}\right) \cdot K_{th} \cdot \left(\frac{1}{T_\infty}\nabla T_\infty\right) \tag{12}$$

The first and the second terms on the right-hand side of Eq. (12) represent the drag force and the thermophoretic force acting on particles, respectively. The drag coefficient C_D and the coefficient K_{th} used in the thermophoretic force term are calculated according to Li and Chen (2002).

Particle energy equations

When in-flight particles are in solid-phase, particle temperature is calculated by

$$\frac{dT}{dt} = \frac{3(q - q_r)}{\rho_p C_{p,s} r_p} \tag{13}$$

When in-flight particles are in melting phase, the temperature of the particles would keep the melting point. Liquid-phase fraction increment within the *i*th time step is calculated by

$$\Delta f_l = \frac{3(q - q_r)}{L_m \rho_p r_p} \Delta t_i \tag{14}$$

When in-flight particles are in liquid-phase, particle temperature is calculated by

$$\frac{dT}{dt} = \frac{3(q - q_r)}{\rho_p C_{p,l} r_p} \tag{15}$$

After particle temperature reaches its evaporation point, particle radius reduces with the time as

$$\frac{dr_p}{dt} = -\frac{q - q_r}{\rho_p L_v} \tag{16}$$

where the specific heat flux q from plasma to the in-flight particles is calculated by

$$q = \beta_1 \beta_2 q_c \tag{17}$$

The factor β_1 and β_2 in Eq. (17) are introduced to correct the Knudsen effect (Chen and Pfender, 1983) and particle evaporation effect (Chen and Pfender, 1982). q_c is the heat flux when no Knudsen effect and evaporation exist, and it is calculated from the following equations for the Nusselt number defined as (Li and Chen, 2002)

$$Nu = \frac{2 q_c r_p}{S_{h\infty} - S_{hw}} \tag{18}$$

$$Nu = 2\left[1 + 0.63 Re_\infty Pr_\infty^{0.8} \left(\frac{Pr_w}{Pr_\infty}\right)^{0.42} \cdot \left(\frac{\rho_\infty \mu_\infty}{\rho_w \mu_w}\right)^{0.52} C^2\right]^{0.5} \tag{19}$$

where S_h is called heat conduction potential and calculated by

$$S_h = \int_{T_0}^{T} \kappa dT \tag{20}$$

where T_0 is an arbitrary reference temperature. The factor C in Eq. (19) is calculated by

$$C = \frac{\left[1 - \left(\frac{h_w}{h_\infty}\right)^{1.14}\right]}{\left[1 - \left(\frac{h_w}{h_\infty}\right)^{2}\right]} \tag{21}$$

The subscripts w and ∞ stand for the particle surface and the gas, respectively. q_r in Eqs. (13)-(16) is the radiative heat loss from the particle surface, which is calculated by

$$q_r = \epsilon \sigma_{st} T_w^4 \tag{22}$$

The differential equations from Eqs. (11)-(16) are solved by fourth-order Runge-Kutta method.

2.3. LTE thermodynamic and transport properties

Chemical composition in plasma under the LTE state is determined by minimizing the Gibbs free energy with RAND method (White *et al*., 1958). Thermodynamic properties are directly calculated from the particle number density and the partition functions. The transport properties are calculated on the basis of Chapman-Enskog approximation (Yos, 1963).

2.4. Computational domain and boundary conditions

Computational domain is composed of plasma torch region and plasma jet region, as shown in Fig. 2. The substrate is not considered in this simulation. The geometry of the plasma torch is decided by reference to the one used by Pershin *et al* (2013). In this study, a structured computational grid is adopted for each of the two regions. The total number of grids is about 600,000 for the plasma torch region and about 200,000 for the plasma jet region. The authors assume that the electromagnetic effects in the plasma jet region can be neglected, and therefore, the governing equations for the electromagnetic field are not solved in the plasma jet region. The boundary condition for each region is defined as follows:

Boundary condition for the plasma torch region shown in Fig. 2(a)

- Cathode surface

$$\frac{\partial p}{\partial n} = 0, T = T_{cathode}, \boldsymbol{u} = \boldsymbol{0}, \phi = \phi_{cathode} \tag{23}$$

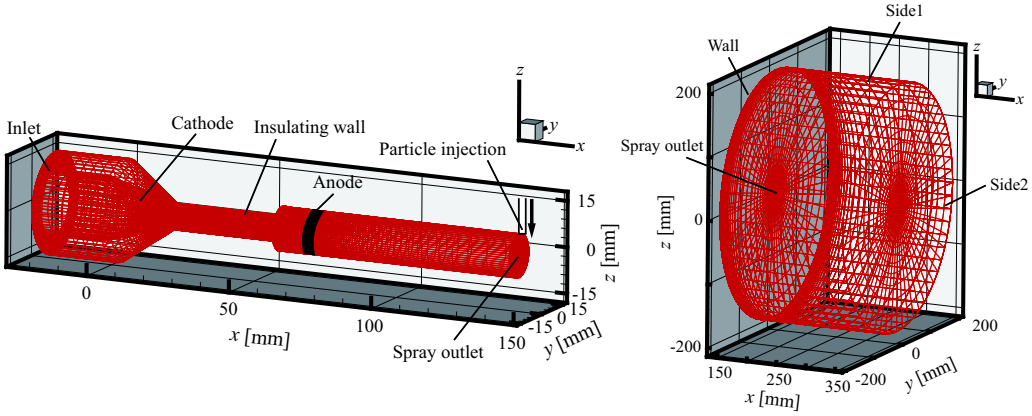

Fig. 2 Computational domain of (a) plasma torch region and (b) plasma jet region.

where $T_{cathode}$ is approximated by a Gaussian profile (Trelles *et al*., 2006),

$$T_{cathode} = T_{cath_{side}} + (T_{cath_{tip}} - T_{cath_{side}})e^{-\left(\frac{r}{R_c}\right)^2} \tag{24}$$

where the cathode radius R_c is set to 6 mm, and also the parameters of $T_{cath_{side}}$ and $T_{cath_{tip}}$, which are used to specify the temperature profiles, are set to 500 and 3653 K, respectively. The value of $T_{cath_{tip}}$ corresponds to the melting point of tungsten.

The electric potential on the cathode $\phi_{cathode}$ is determined so as to satisfy an assigned total current between anode and cathode electrodes.

- Anode surface

The black area shown in Fig. 2(a) corresponds to a ring-shaped anode electrode with the width of 4 mm; it should be noted that the anode shape supposed here is the same as the one used by Pershin *et al* (2013). As the boundary condition on the anode,

$$\frac{\partial p}{\partial n} = 0, T = T_{anode}, \boldsymbol{u} = \boldsymbol{0}, \phi = 0 \tag{25}$$

where T_{anode} is obtained by

$$h_{aw}(T_{anode} - T_{water}) = \kappa\frac{T - T_{anode}}{\Delta n} \tag{26}$$

where h_{aw} is the convective heat-transfer coefficient at the water-cooled anode surface equal to 10^5 W m^{-2} K^{-1} ,which is taken from the previous research (Trelles *et al*., 2006). T_{water} is set to 500 K.

- Insulating wall

$$\frac{\partial p}{\partial n} = 0, T = T_{ins}, \boldsymbol{u} = \boldsymbol{0}, \frac{\partial \phi}{\partial n} = 0 \tag{27}$$

where T_{ins} is obtained by

$$h_{aw}(T_{ins} - T_{water}) = \kappa\frac{T - T_{ins}}{\Delta n} \tag{28}$$

- Center Axis

$$\frac{\partial p}{\partial r} = 0, \frac{\partial T}{\partial r} = 0, \frac{\partial \boldsymbol{u}}{\partial r} = \boldsymbol{0}, \frac{\partial \phi}{\partial r} = 0 \tag{29}$$

- Inlet

$$\frac{\partial p}{\partial n} = 0, T = T_{in}, \frac{\partial \phi}{\partial n} = 0 \tag{30}$$

where T_{in} is inlet gas temperature equal to 300 K. Inlet gas velocity is given by Trelles *et al*. (2006),

$$\boldsymbol{u} = \begin{bmatrix} 2U_{in}\left(1 - \left(\frac{r}{R_a}\right)^2 + (1-k^2)\frac{ln(r/R_a)}{ln(1/k)}\right) / \left(1 + k^2 - \frac{1-k^2}{ln(1/k)}\right) \\ 0 \\ 0 \end{bmatrix} \tag{31}$$

where U_{in} is the parameter to set the volume flow rate to 115 slm and k is defined as the ratio of cathode radius R_c to anode radius R_a as follows:

$$k = \frac{R_c}{R_a} \tag{32}$$

- Spray outlet

$$p = P_0, \frac{\partial T}{\partial n} = 0, \frac{\partial \boldsymbol{u}}{\partial n} = \boldsymbol{0}, \frac{\partial \phi}{\partial n} = 0 \tag{33}$$

where P_0 is the reference pressure equal to 101,325 kPa.

- Periodic boundary

$$\frac{\partial p}{\partial \theta} = 0, \frac{\partial T}{\partial \theta} = 0, \frac{\partial \boldsymbol{u}}{\partial \theta} = \boldsymbol{0}, \frac{\partial \phi}{\partial \theta} = 0 \quad (34)$$

On all of the boundaries, the vector potential $\boldsymbol{A}$ is given by

$$\boldsymbol{A} = \frac{\mu_0}{4\pi} \int_V \frac{\boldsymbol{J}}{|\boldsymbol{r}'|} dV \quad (35)$$

Boundary condition for the plasma jet region shown in Fig. 2(b)

- Spray outlet (corresponding to the inlet of the plasma jet region)

The fluid properties obtained from the computation of the plasma torch region are fixed on this boundary surface.

- Wall

$$\frac{\partial p}{\partial n} = 0, T = T_w, \boldsymbol{u} = \boldsymbol{0} \quad (36)$$

T_w is the wall temperature equal to 300 K.

- Center Axis

$$\frac{\partial p}{\partial r} = 0, \frac{\partial T}{\partial r} = 0, \frac{\partial \boldsymbol{u}}{\partial r} = \boldsymbol{0} \quad (37)$$

- Side1

$$p = P_0, \frac{\partial T}{\partial n} = 0, T = T_0, \frac{\partial \boldsymbol{u}}{\partial n} = \boldsymbol{0} \quad (38)$$

where T_0 is the reference temperature equal to 300 K.

- Side2

$$\frac{\partial p}{\partial n} = 0, \frac{\partial T}{\partial n} = 0, \frac{\partial \boldsymbol{u}}{\partial n} = \boldsymbol{0} \quad (39)$$

- Periodic boundary

$$\frac{\partial p}{\partial \theta} = 0, \frac{\partial T}{\partial \theta} = 0, \frac{\partial \boldsymbol{u}}{\partial \theta} = \boldsymbol{0} \quad (40)$$

2.5. Distribution of externally applied magnetic field

Figure 3 depicts the distribution of externally applied magnetic field around the anode with the maximum external magnetic flux density B_0 of 0.8 T. The effects of the electromagnetic shield and magnetization are negligible as the material of the anode is assumed to be copper which has low magnetic permeability. B_0 is parametrically changed in this simulation with the range of 0 to 0.8 T by adjusting a current density in the coil.

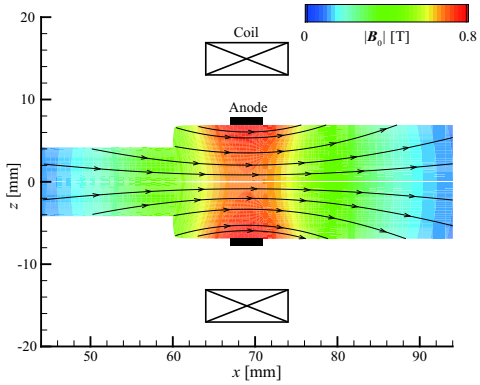

Fig. 3 Distribution of externally applied magnetic field with B_0 = 0.8 T.

2.6. Particle injection condition

Powder material is ZrO_2 and physical properties of ZrO_2 is shown in Table 1. Initial particle radius is 10 μm and initial injection velocity $(u_{px0}, u_{py0}, u_{pz0})$ is (0 m/s, 0 m/s, -20 m/s). Injection point (x_{p0}, y_{p0}, z_{p0}) is (143.2 mm, 0.0 mm, 7.0 mm) shown in Fig. 2(a).

3. Results and discussion

Table 2 presents the operating conditions. Figure 4 shows iso-surfaces of gas temperature (a) with and (b) without externally applied magnetic field (B_0 = 0.8 T) at I = 350 A. When applying externally applied magnetic field of 0.4 T and 0.8 T, the anode arc root continues to rotate and swirl flow is induced in plasma torch. The rotation velocity of 0.8 T is the largest because Lorentz force strongly acts on the arc root in proportion to B_0 with the same current condition. In

Table 1 Physical properties of injected particles.

	ZrO_2
Density, ρ_p [kg/m^3]	5890
Thermal conductivity of solid, $k_{p,s}$ [W/(m·K)]	2.0
Thermal conductivity of liquid, $k_{p,l}$ [W/(m·K)]	3.0
Emissivity, ϵ [−]	0.3
Specific heat of solid, $C_{p,s}$ [J/(kg·K)]	580.0
Specific heat of liquid, $C_{p,l}$ [J/(kg·K)]	713.0
Melting point, T_m [K]	2950.0
Boiling point, T_b [K]	5050.0
Melting latent heat, L_m [kJ/kg]	810
Evaporation latent heat, L_v [kJ/kg]	6000

Table 2 Operating conditions.

Gas	Current [A]	Flow rate [slm]	Externally applied magnetic field [T]
Ar	350	115	0.2
Ar	350	115	0.4
Ar	350	115	0.8

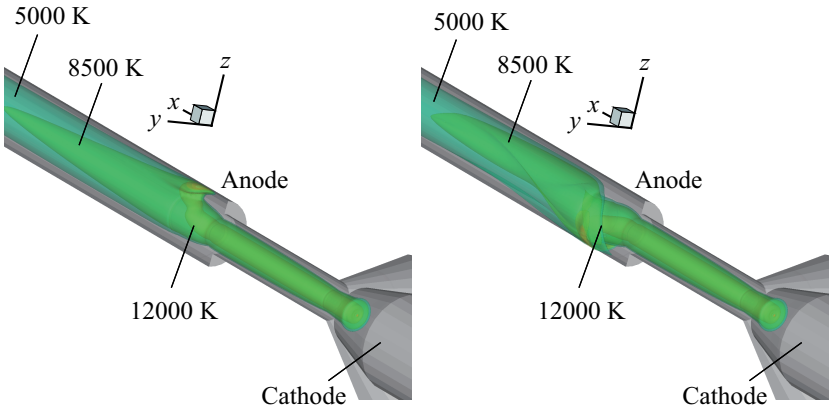

Fig. 4 Iso-surfaces of gas temperature (a) with and (b) without externally applied magnetic field (B_0 = 0.8 T) at I = 350 A.

the case of 0.2 T at 350 A, although the arc rotation movement is observed, the movement is suppressed gradually before the anode arc root revolves one turn. Finally, anode arc root stays on almost the same spot and the rotation movement seems to stop.

Figure 5 shows time evolution of voltage drop with different magnetic field strength at I = 350 A from 0 to 2.5 ms. Larger average voltage drop is obtained after applying external magnetic field for each case. It is expected to generate higher enthalpy plasma jet. This larger voltage drop comes from arc expansion with anode arc root sliding in circumferential direction. For the case of 0.2 T, voltage seems to be saturated after 2 ms. This is because the anode arc rotation movement almost stops, changing the arc radius and arc length little. Voltage fluctuations are observed for applying magnetic field of 0.4 T and 0.8 T. These fluctuations depend on the rotating arc expansion and attachment area where the anode arc root slides. The voltage with 0.4 T tends to be higher than that of 0.8 T in this simulation. This is because the increase in rotating velocity with strengthening magnetic field enhances a heat transfer from the arc to the surrounding gas, so that the region with high electrical conductivities more expands around the arc for B_0 = 0.8 T than for B_0 = 0.4 T. This expansion practically increases the thickness of anode arc root which connects the cathode arc column and the anode arc root, reducing voltage drop. Voltage fluctuations have strong effect on gas velocity at the torch outlet as shown later.

Figure 6 shows the temperature distributions on y-z plane at the outlet with (a) B_0 = 0.8 T and (b) B_0 = 0.2 T of externally applied magnetic field at I = 350 A. For the case of 0.8 T, the rotation of outlet temperature distributions is observed 0.3 ms after applying external magnetic field. Temperature distributions rotate counter-clockwise here. After the arc rotation begins, the gas temperature and the electrical conductivity near anode surface become higher by joule heating and arc rotation velocity gradually increases. The first rotation of temperature distributions at outlet requires about 1.0 ms and the required time for the second to fifth rotation are about from 0.4 ms to 0.5 ms. For the case of 0.2 T, the rotation of

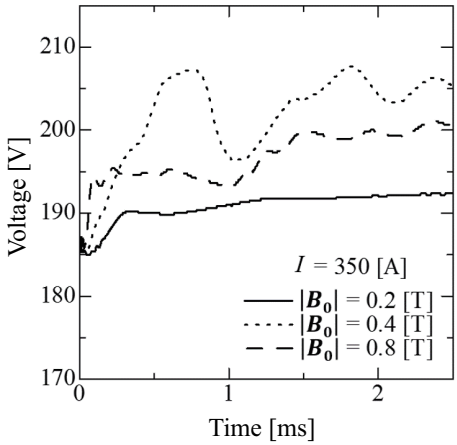

Fig. 5 Time evolution of voltage drop with different magnetic field strength at I = 350 A from 0 to 2.5 ms.

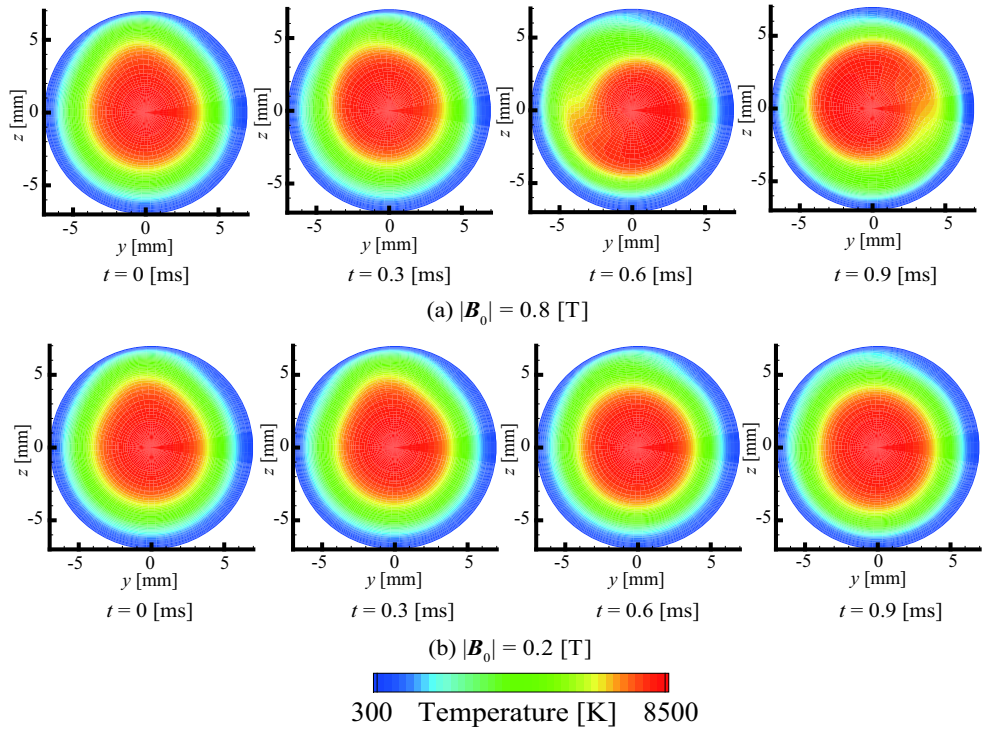

Fig. 6 Temperature distributions with (a) B_0 = 0.8 T and (b) B_0 = 0.2 T.

outlet temperature is hardly observed because the arc rotation movement in plasma torch almost stops after 1 ms.

Figure 7 shows the x-component of gas velocity distributions on y-z plane at the outlet with (a) B_0 = 0.8 T and (b) B_0 = 0.2 T of externally applied magnetic field at I = 350 A. After the application of external magnetic field, the gas velocity at the outlet becomes higher than that without external magnetic field. This increasing of velocity comes from the higher power input by applying the external magnetic field. For the case of 0.8 T, the magnitude of velocity at outlet fluctuates according to the voltage fluctuation in plasma torch. This fluctuation amplitude is over 50 m/s and it is expected to change sprayed particle trajectories and impacting velocities greatly. For the case of 0.2 T, voltage fluctuation is small and the maximum velocity at outlet is almost the same after 0.3 ms.

Figure 8 shows particle trajectories and heating histories without B_0 and with B_0 = 0.8 T at I = 350 A when particle injected time is different. Particle injection condition is all the same for each case. Without externally applied magnetic field B_0, the injected particle goes in the direction parallel to x-axis. After it is heated over melting point, particle is again cooled in front of the plane at x = 195 mm. With externally applied magnetic field B_0, particle trajectories are different according to different injection timing. The y and z component of velocity of swirling flow distorts the particle trajectories.

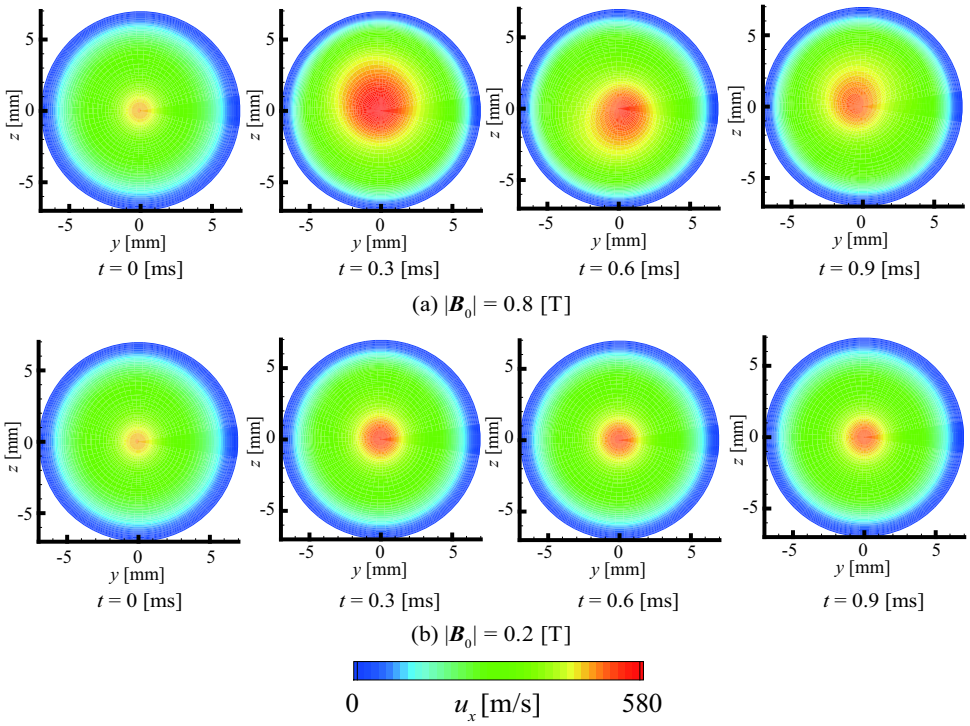

Fig. 7 x-component of gas velocity distributions with (a) B_0 = 0.8 T and (b) B_0 = 0.2 T.

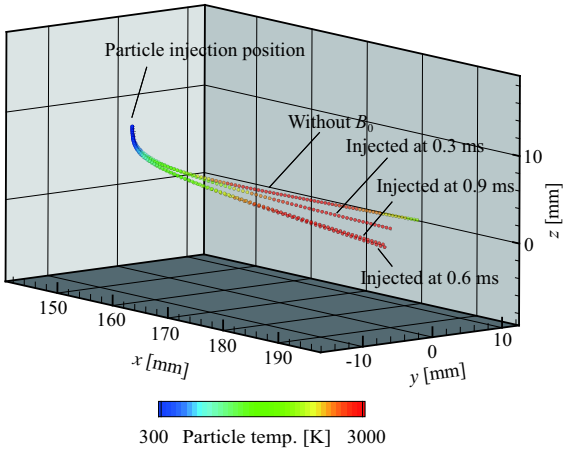

Fig. 8 Particle trajectories and heating histories without B_0 and with B_0 = 0.8 T.

Particle temperature when it goes through the plane at x = 195 mm becomes higher at any injection time compared to that without external magnetic field because higher enthalpy plasma jet is generated by applying magnetic field.

Figure 9 shows particle position and temperature distributions with (a) B_0 = 0.0 T and (b) B_0 = 0.8 T at I = 350 A on y-z plane at x = 195 mm. The total number of 3000 particles are injected into plasma jet within about 2 ms after applying external magnetic field at even time intervals. Particle injection condition is the same except using the standard Gaussian distribution for the initial injection velocity. It is clear that while the particle positions without external magnetic field spread like a circle, those with external magnetic field of 0.8 T spread diagonally. Particles are radially injected into plasma jet around the top edge of spray outlet and this region has the flow velocity of swirling counter-clockwise. This flow mainly carries particles to the substrate, producing diagonal distributions with rotating counter-clockwise. The particles injected just after applying external magnetic field are little affected by the swirling flow, reaching the less deflected positions.

There is also a marked difference in temperature distributions. Particle temperatures in the case without external magnetic field are under melting point and it means that the particles in solid-phase go through the plane of x = 195 mm. With external magnetic field, more than half of particles are heated enough to be over melting point. Applying magnetic field is effective method to produce higher enthalpy plasma jet with reduced operation current.

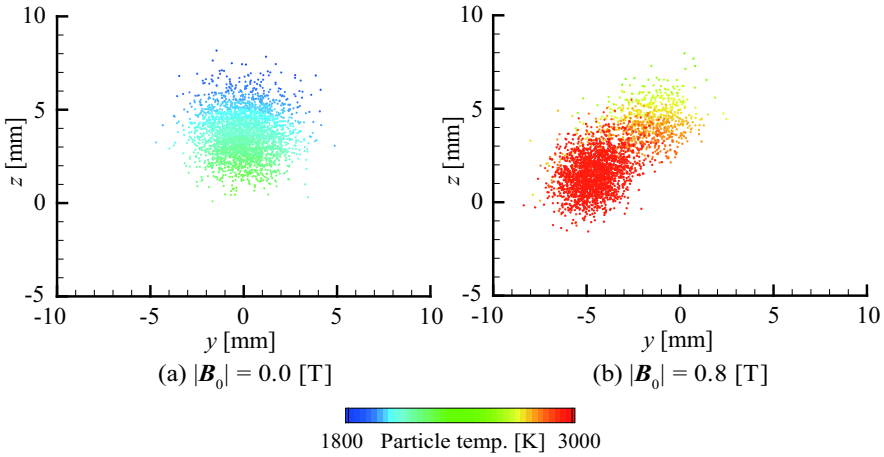

Fig. 9 Particle position and temperature distributions with (a) B_0 = 0.0 T and (b) B_0 = 0.8 T at 350 A on y-z plane (x = 195 mm).

4. Conclusions

Time-dependent MHD simulations of a dc plasma spray with externally applied magnetic field and in-flight particle trajectory analysis are performed in this work. Numerical results show arc rotation induced by the application of external magnetic field generates a swirling plasma jet and also increases the operating voltage and the input power for the spraying process compared to the ones without it. The trajectories of the particles radially injected into the swirling plasma jet are distorted and particle impact positions on the substrate depend on the injection timing of particles. However, the plasma jet with externally applied magnetic field has a higher enthalpy than the one without it under the same current between the electrodes, and therefore the utilization of externally applied magnetic field is useful for impacting the particles with well-molten state on the substrate.

A coil magnet system including a power source was not specified in this work. In our future study, total energy including arc power and power required for the magnet should be considered to clarify the effectiveness of applied magnetic field in the plasma spray process from the view point of energy efficiency.

Nomenclature

$\boldsymbol{A}$: magnetic vector potential [T·m]
$\boldsymbol{B}$: vector of magnetic flux density [T]
$\boldsymbol{B}_0$: vector of external magnetic flux density [T]
C_D : drag coefficient [-]
$C_{p,s}$: solid-phase specific heat of particle material [J/(kg·K)]
$C_{p,l}$: liquid-phase specific heat of particle material [J/(kg·K)]
E_{flu} : specific total energy [J/kg]
e_{flu} : specific internal energy [J/kg]
$\boldsymbol{E}$: electric field vector [V/m]
f_l : liquid-phase fraction [-]
h : gas specific enthalpy [J/kg]
H_{flu} : specific total enthalpy [J/kg]
$\boldsymbol{J}$: electric current density vector [A/m^2]
$k_{p,l}$: thermal conductivity of particle material in liquid phase [W/(m·K)]
$k_{p,s}$: thermal conductivity of particle material in solid phase [W/(m·K)]
L_m : melting latent heat [kJ/kg]
L_v : evaporation latent heat [kJ/kg]
Nu : Nusselt number [-]
$\boldsymbol{n}$: unit vector of normal direction [-]

p : gas pressure [Pa]
Pr : Prandtl number [-]
q : specific heat flux [W/m^2]
q_r : radiative heat loss from particle surface [W/m^2]
$\dot{q}_{rad}$: radiative heat loss [W/m^3]
Re : Reynolds number [-]
R_a : anode radius [m]
R_c : cathode radius [m]
r : coordinate in r-direction
r_p : particle radius [m]
$\boldsymbol{r}'$: displacement vector [m]
S : area of cell interface [m^2]
S_h : heat conduction potential [W/m]
T : temperature [K]
T_w : surface or wall temperature [K]
T_∞ : gas temperature [K]
t : time [s]
Δt_i : the ith time step [s]
$\boldsymbol{u}$: gas velocity vector [m/s]
$\boldsymbol{u}_p$: particle velocity vector [m/s]
V : cell volume [m^3]
$\boldsymbol{x}_p$: position vector of particle [m]
z : coordinate in z-direction

Greek letters

β_1, β_2 : heat flux correction factors due to Knudsen effect and evaporation [-]
ϵ : particle surface emissivity [-]
θ : coordinate in θ-direction
ϕ : electric potential [V]
κ : gas thermal conductivity [W/(m·K)]
μ : gas dynamic viscosity [Pa·s]
μ_0 : permeability of free space [Wb/(A·m)]
π : circular constant [-]
ρ : mass density [kg/m^3]
ρ_p : density of particle material [kg/m^3]
σ : electrical conductivity [S/m]
σ_{st} : Stefan-Boltzmann constant [W/(m^2·K^4)]
$\overline{\overline{\tau}}$: tensor of viscous shear stress [N/m^2]

Acknowledgement

Part of the work was carried out under the Collaborative Research Project of the Institute of Fluid Science, Tohoku University. The calculations were performed using SGI UV 1000 of super-computing system in the Institute of Fluid Science, Tohoku University. The authors especially thank Prof. Javad Mostaghimi for fruitful advices on this study. I would like to thank Dr. Larry Pershin for giving the detailed plasma torch geometry.

References

Alaya, M., Chazelas, C., Mariaux, G. and Vardelle, A., Arc-cathode coupling in the modeling of a conventional dc plasma spray torch, Journal of Thermal Spray Technology, Vol.24, No.1 (2015), pp.3-10.

Chen, X. and Pfender, E., Heat transfer to a single particle exposed to a thermal plasma, Plasma Chemistry and Plasma Processing, Vol.2, No.2 (1982), pp.185-212.

Chen, X. and Pfender, E., Effect of the Knudsen number on heat transfer to a particle immersed into a thermal plasma, Plasma Chemistry and Plasma Processing, Vol.3, No.1 (1983), pp.97-113.

Gutknecht, M. H., Variants of BICGSTAB for matrices with complex spectrum, SIAM Journal on Scientific Computing, Vol.14, No.5 (1993), pp.1020-1033.

Hirayama, S., Fujino, T., Ishikawa, M., Mori, T. and Kawano, H., Numerical study of arc in SF_6 gas circuit breaker with externally applied magnetic field, IEEJ Transactions on Electrical and Electronic Engineering, Vol.11, No.4 (2016), (to be published).

Hu, M., Wan, S., Xia, Y., Ren, Z. and Wang, H., Effect of an external magnetic field on plasma torch discharge fluctuation, Europhysics Letters, Vol.102, No.5 (2013), DOI:10.1209/0295-5075/102/55002.

Li, He-Ping. and Chen, X., Three-dimensional modeling of the turbulent plasma jet impinging upon a flat plate and with transverse particle and carrier-gas injection, Plasma Chemistry and Plasma Processing, Vol.22, No.1 (2002), pp.27-58.

Li, He-Ping. and Pfender, E., Three dimensional modeling of the plasma spray process, Journal of Thermal Spray Technology, Vol.16, No.2 (2007), pp.245-260.

Mostaghimi, J. and Boulos, M. I., Thermal plasma sources: how well are they adopted to process needs?, Plasma Chemistry and Plasma Processing, Vol.35, No.3 (2015), pp.421-436.

Nishiyama, H., Kuzuhara, M., Solonenko, O. P. and Kamiyama, S., Numerical modeling of an impinging and compressible dusted plasma jet controlled by a magnetic field, Plasma Chemistry and Plasma Processing, Vol.19, No.3 (1999), pp.363-381.

Pershin, L., Mitrasinovic, A. and Mostaghimi, J., Treatment of refractory powders by a novel, high enthalpy dc plasma, Journal of Physics D: Applied Physics, Vol.46, No.22 (2013), DOI:10.1088/0022-3727/46/22/224019.

Pfender, E. and Lee, Y. C., Particle dynamics and particle heat and mass transfer in thermal plasmas. Part I. The motion of a single particle without thermal effects, Plasma Chemistry and Plasma Processing, Vol.5, No.3 (1985), pp.211-237.

Pfender, E., Thermal plasma technology: where do we stand and where are we going?, Plasma Chemistry and Plasma Processing, Vol.19, No.1 (1999), pp.1-31.

Sato, T., Shigeta, M. and Nishiyama, H., Mixing and magnetic effects on a nonequilibrium argon plasma jet, International Journal of Thermal Sciences, Vol.40, No.3 (2001), pp.273-278.

Sato, T., Solonenko, O. P. and Nishiyama, H., Numerical simulation of a particle-laden plasma flow in a complex configuration under an electromagnetic field, International Journal of Multiphase Flow, Vol.29, No.3 (2003), pp.461-474.

Shang, S., Guduri, B., Cybulsky, M. and Batra, R. C., Effect of turbulence modulation on three-dimensional trajectories of powder particles in a plasma spray process, Journal of Physics D: Applied Physics, Vol.47, No.40 (2014), DOI:10.1088/0022-3727/47/40/405206.

Trelles, J. P., Pfender, E. and Heberlein, J., Multiscale finite element modeling of arc dynamics in a dc plasma torch, Plasma Chemistry and Plasma Processing, Vol.26, No.6 (2006), pp.557-575.

Trelles, J. P., Computational study of flow dynamics from a dc arc plasma jet, Journal of Physics D: Applied Physics, Vol.46, (2013), DOI:10.1088/0022-3727/46/25/255201.

Wada, Y. and Liou, M. S., A flux splitting scheme with high-resolution and robustness for discontinuities, AIAA paper, (1994), 94-0083.

White, W. B., Johnson, S. M. and Dantzig, G. B., Chemical equilibrium in complex mixtures, The Journal of Chemical Physics, Vol.28, No.5 (1958), pp.751-755.

Wutzke, S. A., Pfender, E. and Eckert, E. R. G., Study of electric-arc behavior with superimposed flow, AIAA Journal, Vol.5, No.4 (1967), pp.707-714.

Wutzke, S. A., Pfender, E. and Eckert, E. R. G., Symptomatic behavior of an electric arc with a superimposed flow, AIAA Journal, Vol.6, No.8 (1968), pp.1474-1482.

Yoon, S. and Jameson, A., Lower-upper symmetric-Gauss-Seidel method for the Euler and Navier-Stokes equations, AIAA Journal, Vol.26, No.9 (1988), pp.1025-1026.

Yos, J. M., Transport properties of nitrogen, hydrogen, oxygen, and air to 30,000 K, AVCO Tech. Mem. RAD-TM-63-7, ASTIA Doc. AD-435-053, (1963).